Inequal responses of drylands to radiative forcing geoengineering methods

Chang-Eui Park[1,2†], Su-Jong Jeong[2], Yuanchao Fan[3*], Jerry Tjiputra[3], Helene Muri[4], Chunmiao Zheng[1*]

[1]School of Environmental Science and Engineering, Southern University of Science and Technology (SUSTech), Shenzhen, China
[2]Graduate School of Environmental Sciences, Seoul National University, Seoul, South Korea
[3]NORCE Norwegian Research Centre and Bjerknes Centre for Climate Research, Bergen, Norway
[4]Industrial Ecology Programme, Department of Energy and Process Engineering, Norwegian University of Science and Technology, Trondheim, Norway

†Present affiliation

*Corresponding author: Chunmiao Zheng (zhengcm@sustech.edu.cn), Yuanchao Fan (yufa@norceresearch.no)

Key Points:

- Impacts of three climate geoengineering methods on global drylands distribution are examined using Earth system model experiments.
- Inequal responses of drylands to individual methods are clearly shown in North America, western Sahara, and Australia.
- Inequality in projected dryland changes under individual geoengineering methods should be considered before any real world implementation.

This article has been accepted for publication and undergone full peer review but has not been through the copyediting, typesetting, pagination and proofreading process which may lead to differences between this version and the Version of Record. Please cite this article as doi: 10.1029/2019GL084210

Abstract

Climate geoengineering has the potential to reduce global warming. However, the nonlinear responses of Earth's large-scale circulation to climate geoengineering can exacerbate regional climate change, with potential inequality risks. We show noticeable inequality in the responses of drylands when three radiative forcing geoengineering (RFG) methodologies – cirrus cloud thinning (CCT), marine sky brightening (MSB), and stratospheric aerosol injection (SAI) – individually reduce the radiative forcing of the Representative Concentration Pathway 8.5 (RCP8.5) scenario using a set of the Norwegian Earth system model (NorESM1-ME) experiments. In North America, CCT and SAI alleviate drylands expansion, whereas, drylands expand further under MSB. CCT induces significantly wetter conditions over the western Sahel. Wetting over Australia is enhanced and prevented by MSB and SAI, respectively. Our results suggest spatially inequal distributions of benefits and harms of individual RFGs on the projected distribution of drylands, which should be considered before any real-world application of such RFGs.

Plain Language Summary

Climate geoengineering has the potential to reduce global warming levels significantly, according to modelling experiments. However, regional impacts of individual climate geoengineering methods are inequal, raising concerns about fairness of negative side effects of such methods. Here, impacts of climate geoengineering on the global distribution of drylands are projected using an Earth system model, NorESM1-ME. Three geoengineering methods are adopted: cirrus cloud thinning (CCT), marine sky brightening (MSB), and stratospheric aerosol injection (SAI). All methods commonly reduce about 2 °C of global warming in the late 21st century relative to the high CO_2 emission scenario, Representative Concentration Pathway 8.5. Drylands respond differently to individual methods, especially in North America, the western Sahel, and Australia. In North America, CCT and SAI alleviate drylands expansion, whereas, the expansion of drylands is intensified under MSB. CCT notably reduces drylands expansion over the western Sahel. The reduction of drylands in Australia is enhanced by MSB due to atmospheric circulation changes, but prevented by SAI. Our results suggest that climate geoengineering can exacerbate drylands expansion in some regions despite potential alleviation in other regions. Such inequalities should be considered if RFGs for real-world applications to mitigate global warming were ever to be considered.

1 Introduction

The idea of altering the Earth's radiative budget through engineered approaches (i.e., RFG) has been proposed to mitigate anthropogenic greenhouse gas-induced warming [e.g., *Tilmes et al.,* 2013; *Lawrence et al.,* 2018]. Three RFG methodologies based on aerosols have been widely discussed: CCT, MSB, and SAI [*Muri et al.,* 2018]. CCT emits more outgoing longwave radiation (OLR) by reducing the number of ice crystals in cirrus clouds, which trap the OLR [*Mitchell and Finnegan,* 2009; *Muri et al.,* 2014]. MSB and SAI act to reduce incoming solar radiation reaching the Earth's surface. The purpose of MSB is to increase reflected solar radiation by spreading bright particles that could act as cloud condensation nuclei into the low-level atmosphere over the oceans [*Twomey,* 1977; *Latham,* 1990; *Partanen et al.,* 2012]. SAI reflects incoming solar radiation by creating a layer of reflective aerosols in the lower stratosphere [*Crutzen,* 2006; *Benduhn et al.,* 2016]. Simulations of global climate models show that the three RFGs have enough potential to lower the RCP8.5 global warming level to a warming level similar to that under RCP4.5 and even to a 1.5 °C warming threshold [*Kravitz et al.,* 2015; *MacMartin et al.,* 2018]. In contrast to their consistent cooling potentials, individual RFGs induce different impacts on the Earth's large-scale circulation, raising concerns over inequality risks of RFG impacts on regional climate and hydrological cycle [*Irvine et al.,* 2010; *Crook et al.,* 2015; *Irvine et al.,* 2019; *Wei et al., 2018*], as well as the distribution and dynamics of climate regimes, such as drylands. Many assessments have examined the potential of RFGs to induce changes in the regional climate, especially precipitation (P) [*Niemeier et al.,* 2013; *Kristjánsson et al.,* 2015; *Stjern et al.,* 2018], but the response of drylands to individual RFGs remains unexplored.

Drylands, defined as areas where the amount of precipitation is insufficient for maintaining evapotranspiration from surfaces, occupy 41% of the land surface, and provide residences for more than one-third of the world's population [*Middleton and Thomas,* 1997]. Due to infertile soil and consequent fragile ecosystems, drylands are the most vulnerable areas to degradation and desertification induced by climate changes and human activities [*Middleton and Thomas,* 1997]. The area of total drylands generally increases in warmer climates with distinct regional responses [*Feng and Fu,* 2013; *Huang et al.,* 2016], indicating that drylands are susceptible to both global warming and local climate changes. RFGs have the potential to either mitigate dryland expansion by reducing global warming and creating wetter meteorological conditions in some places, or indeed exacerbate dryland expansion in others. Such aspects of RFG are largely unexplored to date. Thus, understanding the RFG

consequences in regional drylands is a necessary prerequisite for decision makers when considering the implementation of RFG in the real world.

We quantify and compare the projected impacts of CCT, MSB, and SAI on the expansion of drylands based on an experimental set using NorESM1-ME, a fully-coupled Earth system model. Three RFGs are implemented individually on top of the RCP8.5 scenario, such that the global net radiative forcing is reduced a magnitude comparable to RCP4.5 over an intervention period of 81 years; from 2020 to 2100. Then, a 50-year extension is continued for each case without RFGs for 2101-2150 to examine any abrupt termination effects. The distribution of drylands and their spatiotemporal changes are examined using a ratio of P to potential evapotranspiration (PET), i.e., P/PET, known as aridity index (AI) [*Middleton and Thomas,* 1997; *Feng and Fu,* 2013].

2 Materials and Methods

2.1 Model and experiments

NorESM1-ME, a fully coupled climate carbon-cycle model, is used to perform all experiments (Table 1). This model has participated in many experiments of phase 5 of the Coupled Model Intercomparison Project (CMIP5) and contributed to the Intergovernmental Panel on Climate Change Fifth Assessment Report. Model experiments are performed at the following horizontal resolutions: 1.9° × 2.5° in latitude and longitude for atmosphere and land with 26 vertical levels of atmosphere in a hybrid-sigma coordinate, and a 1° × 1° horizontal resolution for the ocean with 53 isopycnic layers. Details of the model processes are described in in *Bentsen et al.* [2013] and *Tjiputra et al.* [2013].

Standard CMIP5 historical simulation for 1850-2005 and future climate simulations following the RCP4.5 and RCP8.5 scenarios for 2006-2100 were carried out [*Meinshausen et al.*, 2011; *Taylor et al.*, 2011]. CCT, MSB, and SAI techniques were separately applied to the RCP8.5 scenario to reduce the radiative forcing of RCP8.5 to that of RCP4.5 [*Muri et al.*, 2018]. The three RFGs are implemented over a planetary scale for 81 years from 2020 to 2100, and then abruptly terminated. The forcing strengths are not spatially uniform and increased with time from 2020 to 2100 to achieve the atmospheric radiative imbalance comparable to RCP4.5 in the year 2100. For each RFG, three ensemble members were integrated with a small perturbation of initial conditions at the beginning of each experiment. To examine the termination effects, a 50-year additional experiment was continued after RFG cut-offs following the extended concentration pathway 8.5 [*Meinshausen et al.*, 2011]. All

experiments are performed with interactive biogeochemical processes and prescribed anthropogenic CO_2 emissions.

To realize CCT, we adopt an idealized ice cloud thinning method, which increases the terminal velocity of all ice crystals for temperatures colder than −38 °C [*Muri et al.,* 2014], because of relatively simple parameterizations of ice cloud microphysics in NorESM1-ME, which is typical for ESMs. This simple method shows a comparable ability to reduce the radiative forcing at the top of the atmosphere (ToA) and surface temperature to that of a more complex method based on increasing ice nuclei in cirrus clouds [*Gasparini et al.,* 2017]. The MSB is implemented in the model by uniformly increasing the emission of sea salt particles in the accumulation mode at the ocean surface within latitudes 45°S-45°N [*Alterskjær, K. and Kristjánsson,* 2013; *Muri et al.,* 2018]. The accumulation mode is known to be the most efficient for increasing shortwave cloud forcing [*Alterskjær and Kristjánsson,* 2013]. For SAI, a prescribed dataset for the injected sulfur dioxide (SO_2) layer in the stratosphere was applied to NorESM1-ME because the model doesn't have an interactive stratospheric aerosol module [*Muri et al.,* 2018]. The dataset provides the distribution of injected SO_2 and its optical properties. SO_2 is injected in the tropics, and its injection strength increases from 5 Tg SO_2 yr^{-1} in 2050 to 20 Tg SO_2 yr^{-1} in 2100. For a more detailed description of the RFG implementation and model experiments, see *Muri et al.* [2018].

2.2 Drylands definition and PET calculation

Drylands are defined as regions with AI (P/PET) < 0.65 and are divided into hyperarid (AI<0.05), arid (0.05≤AI<0.2), semiarid (0.2≤AI<0.5), and dry subhumid (0.5≤AI<0.65) regions [*Middleton and Thomas,* 1997]. PET is estimated using a standardized version of the Penman-Monteith model for a reference crop defined as a hypothetical crop assumed to have a height of 0.12 m, surface resistance of 70 s m^{-1}, and an albedo of 0.23 [*Allen et al.,* 1998]. We obtained surface air temperature (SAT), available energy, relative humidity (Rh), and 10 m height wind speed (WS) from NorESM1-ME outputs for calculating PET. The available energy is defined as subtracting the heat flux into the ground (G) from net radiation at the surface (R_n), i.e., R_n–G. Here, we replace the R_n–G by the sum of latent heat and sensible heat [*Lin et al.,* 2018]. Note that this Penman-Monteith PET denotes atmospheric water demand, thus the AI represents atmospheric aridity [*Greve et al.,* 2017].

2.3 Climatology bias correction

We performed a climatology bias correction on NorESM1-ME outputs using the observation dataset and methodology introduced in *Feng and Fu* [2013] to certify the consistency between the observation and model. To match with the observation dataset, all NorESM1-ME outputs are downscaled from 1.9° × 2.5° to 0.5° × 0.5° horizontal resolution. Five climate parameters relevant to AI – P, SAT, downwelling solar radiation, Rh, and WS – are adjusted to the monthly climatology of 1961-1990 derived from the observation, such that the adjusted parameters have the same climatology to the observation for the 1961-1990 period. Anomalies of the five parameters relative to the modeled climatology of 1961-1990 are first computed and then regridded into half-degree horizontal resolution. Finally, we obtained the adjusted climate parameters by adding modeled anomalies at the half-degree to the observed climatology for 1961-1990. The adjusted P, SAT, Rh, and WS are directly used to estimate the bias-corrected AI. The R_n–G is corrected by subtracting the difference of modeled and observed downwelling solar radiation for the period of 1961-1990 because the R_n–G is denoted by the sum of latent heat and sensible heat. The spatial distribution of the adjusted AI compares well with that derived from the Climate Research Unit Time Series 4.03 (CRUTS4) [*Harris et al.*, 2014] and Climate Prediction Center (CPC) [*Feng and Fu*, 2013] (Figure S1). Note that the bias correction procedure retains the temporal variation and long-term trends of NorESM1-ME simulated fields [*Ramirez-Villegas and Jarvis*, 2010; *Feng and Fu*, 2013].

3 Results

Temporal anomalies of the 20-year running mean SAT, annual P and PET, and AI relative to the 1986-2005 climatology averaged over the land surface within latitudes of 60°S-60°N obtained from NorESM1-ME are generally consistent with those of CRUTS4 for 1950-2005, indicating that temporal variability of simulated climate parameters is similar to that of the observations (Figure 1). SAT shows consistent cooling potential for all three RFGs from 2020 to 2100; however, the responses of P and PET to the individual RFGs are different (Figures 1a-1c). CCT and SAI induce the largest and smallest increments of P, respectively, which are higher than RCP8.5 and lower than RCP4.5 (Figure 1b). The increase in P under MSB is less than that under RCP8.5. The increases in PET under all three RFGs are smaller and larger than that under RCP8.5 and RCP4.5, respectively, in the order of CCT, MSB, and SAI from largest to smallest (Figure 1c). Consequently, less decrease in AI is consistently observed under CCT, MSB and SAI than under RCP8.5 despite the different responses of P

and PET to individual RFGs (Figure 1d). After the termination of RFGs at the beginning of 2101, changes in all these climate parameters revert to those projected under RCP8.5 within 25 years.

Projected areal changes in the 20-year running mean of total drylands and four dryland types derived from the CRUTS4 for 1950-2018, Historical scenario for 1950-2005, RCP4.5 for 2006-2100, and RCP8.5, CCT, MSB, and SAI for 2006-2150 are presented in Figure 2. For the historical period, the total area of simulated drylands is less than that derived from CRUTS4 by 3.0×10^6 km^2 (Figure 2a). The area of hyper-arid and arid regions is larger in CRUTS4 than NorESM1-ME (Figures 2b and 2c). In contrast, NorESM1-ME shows a larger area of semiarid and dry subhumid regions (Figures 2d and 2e). These gaps between CRUTS4 and NorESM1-ME are caused by less AI from NorESM1-ME than that from CRUTS4 over the existing drylands and their boundary regions (Figure S2). The area of total drylands is increased by 2.7×10^6 km^2 and 6.8×10^6 km^2 in 2081-2100 relative to 1986-2005 under the RCP4.5 and RCP8.5 scenarios, respectively (Figure 2a and Table S1), which are comparable to results in the previous studies [*Feng and Fu*, 2013]. When CCT, MSB, and SAI is implemented, the drylands expansion under RCP8.5 is alleviated by 2.3×10^6 km^2, 1.9×10^6 km^2, and 2.8×10^6 km^2 for 2081-2100, which are 33.8%, 27.9%, and 41.2% of the increase in total drylands under RCP8.5 for the same period, respectively, but responses of individual types of dryland to each RFGs are different (Figure 2a and Table S1). Less area of hyper-arid and arid regions under CCT and MSB explains the mitigation of drylands expansion under RCP8.5 (Figures 2b and 2c). SAI mainly reduces the expansion of semiarid and dry subhumid regions relative to RCP8.5 (Figures 2d and 2e). After the termination, changes in total drylands and respective four subtypes are adjusted to those under RCP8.5.

Different responses of each dryland types between RCP8.5 and individual RFGs suggest the spatially varying responses of drylands. Figure 3 illustrates regions experiencing dryland type changes to drier and wetter from 2081-2100 for RCP4.5 and RCP8.5 relative to 1986-2005 climatology (Figures 3a and 3b), also for CCT, MSB, and SAI relative to 2081-2100 climatology derived from RCP8.5 (Figures 3c-3e). Overall, changes in dryland types mainly occur along boundary regions of existing drylands according to changes in AI (Figures 3, S1, and S3), which is consistent with behavior found in previous results [*Feng and Fu,* 2013; *Huang et al.,* 2016]. Under RCP4.5 and RCP8.5, more regions are projected to become drier than wetter in all experiments, resulting in the net expansion of drylands

(Figures 2a, 3a, and 3b). Dryland type changes to both drier and wetter are relatively large under RCP8.5, and moderate under RCP4.5 (Figures 3a and 3b). RFGs generally induce type changes to wetter relative to RCP8.5, as shown in temporal changes despite the drying in some regions according to individual RFGs (Figures 3c-3e).

Under the RCP8.5 scenario, changes to drier types mainly occur over central North America (CNA), central America (CAM), South America (SAM), the Mediterranean (MED), southern Africa (SAF), and central Asia (CAS), whereas western Sahel (WSH) and Australia (AUS) experience changes to wetter types (Figure 3b). RFGs generally induce type changes to wetter relative to RCP8.5, resulting in the previously shown alleviation of drylands expansion by RFGs despite drying in some regions (Figures 2a and 3c-3e). RFGs show, in some regions, common effects on drylands, for example, reduction of drylands expansion over CAM, MED, and SAF (Figures 3c-3e and S4). However, a notable difference in the impacts of individual RFGs on drylands is shown over CNA, WSH, and AUS. In CNA, regions with changes to the drier type are increased by the MSB methodology, whereas both CCT and SAI significantly reduce the dryland expansions (Figures 3c-3e and S4). CCT induces relatively strong wetting over WSH (Figure 3c and S4). The wetting in AUS under RCP8.5 is enhanced by MSB, but is constrained by both CCT and SAI (Figures 3c-3e and S4).

Unequal distributions of RFG impacts on drylands are explained by changes in AI and relevant climate parameters. Figure 4 shows the areal changes in drylands types as well as differences in AI and respective varying contributions of P, SAT, R_n−G, Rh, and U_2 to AI changes for 2081-2100 between individual RFGs and RCP8.5 over three regions. More details on estimating the individual contributions of P, SAT, R_n−G, Rh, and U_2 to overall AI changes are provided in Appendix A of *Fu and Feng* (2014) and Appendix A of *Lin et al.* (2018). Note that positive contributions indicate that changes in relevant variable increase AI, and vice versa. In CNA, MSB largely increases type changes to drier by 0.9×10^6 km^2 according to the decrease in AI (Figures 4a and 4b). Negative anomaly of P contribution governs the drying (Figure 4c). Whereas, significant increase in AI under CCT and SAI commonly enhances type changes to wetter by 0.7×10^6 km^2 (Figures 4a and 4b). The wetting due to CCT is mainly caused by positive anomaly of P and SAT contributions (Figure 4c). Increase in contributions of SAT, R_n−G, and Rh enhances AI under SAI. In WSH, CCT and MSB induce significant increase in type changes to wetter by 1.5×10^6 km^2 and 0.9×10^6 km^2, respectively, whereas, SAI shows both type changes to drier and wetter up

to 0.6×10^6 km^2 and 0.3×10^6 km^2, respectively (Figure 4d). Under CCT, the increase in contribution of P leads to the AI increase and wetting (Figures 4d-4f). The increase in AI under MSB is caused by the increase in contributions of P, SAT, and R_n−G (Figures 4e and 4f). Under SAI, negative contribution of P is offset by positive contributions of both SAT and R_n−G, leading to slight changes in AI (Figures 4e and 4f). In AUS, wetting and drying under MSB and SAI are connected to the increase and decrease in AI, respectively (Figures 4g and 4h). The contrasting effects of MSB to SAI are generally explained by opposite changes in P contributions (Figure 4i). Note that spatial distributions of changes in P, SAT, R_n−G, and Rh are also consistent with respective contributions to AI changes over individual regions (Figures S5-S7).

4 Discussions and conclusions

This study primarily determines the responses of drylands to three individual RFGs, which shows similar potential to cool the Earth. In general, adopting three RFG methodologies alleviates the expansion of drylands under the RCP8.5 scenario because the decrease in global mean temperature due to RFGs generally reduces the climate changes according to the increase in atmospheric concentration of greenhouse gases [*Lawrence et al.*, 2018; *Irvine et al.*, 2019]. For example, in MED and SAF, both decrease in P and increase in PET under RCP8.5 are mitigated by the three RFGs, resulting in alleviation of drylands expansion (Figure S8). However, unequal responses of drylands to individual RFG methodologies are substantial over CNA, WSH, and AUS. This regional disparity in RFG impacts on dryland distribution is fundamentally induced by changes in the large-scale circulation originating from the radiative imbalance. When CCT is implemented, thinner cirrus clouds increase incoming solar radiation and strengthens radiative cooling in the upper troposphere. Due to the lower heat capacity of the land, increases in surface air temperature according to the increased solar radiation is larger in the Northern Hemisphere than in the Southern Hemisphere, resulting in northward shift in the intertropical convergence zone (ITCZ) [*Muri et al.*, 2014; 2018]. Also, the warming in lower troposphere and cooling in upper troposphere promote convections and enhance the global hydrological cycle [*Kristjánsson et al.*, 2015]. The cooling over the ocean surface by the MSB leads to bimodal patterns between tropical and subtropical North Pacific [*Lauvset et al.*, 2017]. These changes enhance convective activities over the western Pacific and eastern Indian Ocean, which alters the Pacific Walker circulation similarly to that under a La Ninã event [*Niemeier et al.*, 2013;

Stjern et al., 2018]. Under SAI, in contrast, the decreased incoming solar radiation and surface cooling combined with heating of the upper troposphere from the stratospheric aerosol layer, generally reduces the vertical temperature gradient (increase in static stability) and hence vertical motion in the troposphere [*Ferraro et al.,* 2014*; Lawrence et al.,* 2018]. These dominant features in the large-scale circulation changes can explain the regional variability in dryland responses. For example, under CCT, the northward shift in convection that occurred in tropical Atlantic is related to the significant wetting over WSH. The La Ninã- and El Ninõ-like patterns of changes in precipitation under MSB and SAI are directly connected to wetting and drying over AUS, respectively.

Our results are drawn by a suitable set of fully coupled Earth system model experiments; however, some limitations remain. Our simplified methods for implementing individual RFGs may overlook many uncertainties related to the complex feedback of aerosols, clouds, and climate. Single model experiments are limited in their ability to provide robust results, although NorESM1-ME can reasonably simulate the responses of the global hydrological cycle to global warming and volcanic eruptions [*Bethke et al.,* 2017]. A series of studies were also conducted based on NorESM1-ME that show insightful findings on climate, carbon, and water cycle impacts of the individual RFGs [*Muri et al.,* 2014; *Kristjánsson et al.,* 2015; *Tjiputra et al.,* 2016; *Lauvset et al.,* 2017; *Muri et al.,* 2018]. Constant surface resistance in the PET calculation ignores the hydrological implications of the vegetation response to unabated CO_2 emission and regional climate change under different RFGs, which can simulate drier conditions in the warmer climate [*Yang et al.,* 2019]. However, our results clearly show different responses of drylands to individual RFGs; therefore, continued studies on various aspects of inequality risks are needed prior to any consideration of actual implementation of RFGs.

Acknowledgments, and Data

High-resolution gridded datasets provided by the Climate Research Unit for this research are available in these in-text data citation references: Harris et al. [2014] (https://crudata.uea.ac.uk/cru/data/hrg/). Climate Prediction Center (CPC) observation dataset for this research are included in this paper: Feng and Fu [2013]. All climate simulation dataset using NorESM1-ME are available upon request to authors.

Chang-Eui Park was supported by Korea Research Fellowship Program through the National Research Foundation of Korea (NRF) funded by the Ministry of Science and ICT (2019H1D3A1A01071022). Su-Jong Jeong was supported by Creative-Pioneering Researchers Program through Seoul National University (SNU). Yuanchao Fan was supported by the Bjerknes Centre Fast-Track Initiative 2018 (Project no. 808011) and the European Union Horizon 2020 Project CRESCENDO funded by program SC5-01-2014:

Advanced Earth-System Models (grant agreement 641816). Jerry Tjiputra acknowledges Research Council of Norway (RCN) funded project COLUMBIA (205268). RCN grants 229760/E10, 261862/E10, and 237917 funded Helene Muri. The simulations were performed on resources provided by UNINETT Sigma2–the National Infrastructure for High Performance Computing and Data Storage in Norway, accounts nn9182k, nn9448k, NS2345K, and NS9033K. We deeply appreciate Dr. Song Feng sharing the observation dataset introduced in *Feng and Fu* [2013].

The authors declare no competing financial interests.

References

Allen, R. G., L. S. Pereira, D. Raes, and M. Smith (1998), Crop evapotranspiration – guidelines for computing crop water requirements – FAO Irrigation and drainage Paper 56 (FAO).

Alterskjær, K., and J. E. Kristjánsson (2013), The sign of the radiative forcing from marine cloud brightening depends on both particle size and injection amount, Geophys. Res. Lett., 40, 210-215, doi:10.1029/2012GL054286.

Alterskjær, K. et al. (2013), Sea-salt injections into the low-latitude marine boundary layer: The transient response in three Earth system models, J. Geophys. Res. Atmos., 118, 12195-12206, doi:10.1002/2013JD020432.

Bala, G., K. Caldeira, R. Nemani, L. Cao, G. Ban-Weiss, and H.-J. Shin (2010), Albedo enhancement of marine clouds to counteract global warming: Impacts on the hydrological cycle, Clim. Dyn., 37, 915-931, doi:10.1007/s00382-010-0868-1.

Bethke, I. et al. (2017), Potential volcanic impacts on future climate variability, Nature Clim. Change, 7, 799-805, doi:10.1038/nclimate3394.

Benduhn, F., J. Schallock J, and M. G. Lawrence (2016), Early growth dynamical implications for the steerability of stratospheric solar radiation management via sulfur aerosol particles, Geophys. Res. Lett., 43, 9956-9963, doi:10.1002/2016GL070701.

Bentsen, M. et al. (2013), The Norwegian Earth System Model, NorESM1-M – Part 1: Description and basic evaluation of the physical climate, Geosci. Model Dev., 6, 687-720, doi:10.5194/gmd-6-687-2013.

Crook, J. A., L. S. Jackson, S. M. Osprey, and P. M. Forster (2015), A comparison of temperature and precipitation responses to different Earth radiation management geoengineering schemes, J. Geophys. Res. Atmos., 120, 9352-9373, doi:10.1002/2015JD023269.

Crutzen, P. J. (2006), Albedo Enhancement by Stratospheric Sulfur Injections: A Contribution to Resolve a Policy Dilemma? Climatic Change, 77, 211-219, doi:10.1007/s10584-006-9101-y.

Feng, S., and Q. Fu (2013), Expansion of global drylands under a warming climate, Atmos. Chem. Phys., 13, 10081-10094, doi:10.5194/acp-13-10081-2013.

Ferraro, A.J. and Griffiths, H.G., 2016. Quantifying the temperature-independent effect of stratospheric aerosol geoengineering on global-mean precipitation in a multi-model ensemble. Environmental Research Letters, 11(3), p.034012.

Fu, Q., and S. Feng (2014), Responses of terrestrial aridity to global warming, J. Geophys. Res. Atmos., 119, 7863-7875, doi:10.1002/2014JD021608.

Gasparini, B., S. Münch, L. Poncet, M. Feldmann, and U. Lohmann (2017), Is increasing ice crystal sedimentation velocity in geoengineering simulations a good proxy for cirrus cloud seeding? Atmos. Chem. Phys., 17, 4871-4885, doi:10.5194/acp-17-4871-2017.

Greve, P., M. L. Roderick, and S. I. Seneviratne (2017), Simulated changes in aridity from the last glacial maximum to 4xCO2, Environ. Res. Lett., 12, 114021, doi:10.1088/1748-9326/aa89a3.

Harris, I., P. D. Jones, T. J. Osborn, and D. H. Lister (2014), Updated high-resolution grids of monthly climatic observations – the CRU TS3.10 Dataset, Int. J. Climatol., 34, 623-642, doi:10.1002/joc.3711.

Huang, J., H. Yu, X. Guan, G. Wang, and R. Guo (2016), Accelerated dryland expansion under climate change, Nat. Clim. Change, 6, 166-171, doi:10.1038/nclimate2837.

Irvine, P. J., A. J. Ridgwell, and D. J. Lunt (2010), Assessing the regional disparities in geoengineering impacts, Geophys. Res. Lett., 37, L18702, doi:10.1029/2010GL044447.

Irvine, P. et al. (2019), Halving warming with idealized solar geoengineering moderates key climate hazards, Nat. Clim. Change, 9, 295-299, doi:10.1038/s41558-019-0398-8.

Kravitz, Ben et al. (2015), The Geoengineering Model Intercomparison Project Phase 6 (GeoMIP6): simulation design and preliminary results, Geosci. Model Dev., 8, 3379-3392, doi:10.5194/gmd-8-3379-2015.

Kristjánsson, J. E., H. Muri, and H. Schmidt (2015), The hydrological cycle response to cirrus cloud thinning, Geophys. Res. Lett., 42, 10807-10815, doi:10.1002/2015GL066795.

Latham, J. (1990), Control of global warming? Nature, 347, 339-340, doi:10.1038/347339b0.

Lauvset, S. K., J. Tjiputra, and H. Muri (2017), Climate engineering and the ocean: effects on biogeochemistry and primary production, Biogeosciences, 14, 5675-5691, doi:10.5194/bg-14-5675-2017.

Lawrence, M. G. et al. (2018), Evaluating climate geoengineering proposals in the context of the Paris Agreement temperature goals, Nat. Comms., 9, 3734, doi:10.1038/s41467-018-05938-3.

Lin, L., A. Gettelman, Q. Fu, and Y. Xu (2018), Simulated differences in 21st century aridity due to different scenarios of greenhouse gases and aerosols, Climatic Change, 146, 407-422, doi:10.1007/s10584-016-1615-3.

MacMartin, D. G., K. L. Ricke, and D. W. Keith (2018), Solar geoengineering as part of an overall strategy for meeting the 1.5 °C Paris target, Phil. Trans. R Soc. A, 376, 20160454, doi:10.1002/2016EF000418.

Meinshausen, M. et al. (2011), The RCP greenhouse gas concentrations and their extensions from 1765 to 2300, Climatic Change, 109, 213, doi:10.1007/s10584-011-0156-z.

Middleton, N., and D. Thomas (1997), World Atlas of Desertification (Oxford Univ. Press).

Mitchell, D. L., and W. Finnegan (2009), Modification of cirrus clouds to reduce global warming, Environ. Res. Lett., 4, 045102, doi:10.1088/1748-9326/4/4/045102.

Muri, H., J. E. Kristjánsson, T. Storelvmo, and M. A. Pfeffer (2014), The climatic effects of modifying cirrus clouds in a climate engineering framework, J. Geophys. Res. Atmos., 119, 4174-4191, doi:10.1002/2013JD021063.

Muri, H. et al. (2018), Climate Response to Aerosol Geoengineering: A Multimethod Comparison, J. Clim., 16, 6319-6340, doi:10.1175/JCLI-D-17-0620.1.

Niemeier, U., H. Schmidt, K. Alterskjær, and J. E. Kristjánsson (2013), Solar irradiance reduction via climate engineering: Impact of different techniques on the energy balance and the hydrological cycle, J. Geophys. Res. Atmos., 118, 11905-11917, doi:10.1002/2013JD020445.

Niemeier, U., and C. Timmreck (2015), What is the limit of climate engineering by stratospheric injection of SO_2? Atmos. Chem. Phys., 15, 9129-9141, doi:10.5194/acp-15-9129-2015.

Partanen, A.-I. et al. (2012), Direct and indirect effects of sea spray geoengineering and the role of injected particle size, J. Geophys. Res. Atmos., 117, D02203, doi:10.1029/2011JD016428.

Ramirez-Villegas, J., and A. Jarvis (2010), Downscaling global circulation model outputs: the delta method decision and policy analysis working paper No. 1, International Center for Tropical Agriculture, CIAT, Cali, Colombia.

Stjern, C. W. et al. (2018), Response to marine cloud brightening in a multi-model ensemble, Atmos. Chem. Phys., 18, 621-634, doi:10.5194/acp-18-621-2018.

Taylor, K. E., R. J., Stouffer, and G. A. Meehl (2011), An Overview of CMIP5 and the Experiment Design, Bull. Amer. Meteor. Soc., 93, 485-498, doi10.1175/BAMS-D-11-00094.1.

Tjiputra, J. F. et al. (2013), Evaluation of the carbon cycle components in the Norwegian Earth System Model (NorESM), Geosci. Model Dev., 6, 301-325, doi:10.5194/gmd-6-301-2013.

Tjiputra, J. F., A. Grini, and H. Lee (2016), Impact of idealized future stratospheric aerosol injection on the large-scale ocean and land carbon cycles, J. Geophys. Res. Biogeoscience, 121, 2-27, doi:10.1002/2015JG003045.

Tilmes, S. et al. (2013), The hydrological impact of geoengineering in the Geoengineering Model Intercomparison Project (GeoMIP), J. Geophys. Res. Atmos., 118, 11036-11058, doi:10.1002/jgrd.50868.

Twomey, S. (1977), The Influence of Pollution on the Shortwave Albedo of Clouds, J. Atmos. Sci., 7, 1149-1152, doi:10.1175/1520-0469(1977)034<1149:TIOPOT>2.0.CO;2.

Wei, L., Ji, D., Miao, C., Muri, H. and Moore, J.C., 2018. Global streamflow and flood response to stratospheric aerosol geoengineering. Atmospheric Chemistry and Physics, 18(21), pp.16033-16050.

Yang, Y., M. L. Roderick, S. Zhang, S., T. R. McVicar, and R. J. Donohue, Hydrologic implications of vegetation response to elevated CO_2 in climate projections, Nat. Clim. Change, 9, 44-48, doi:10.1038/s41558-018-0361-0.

Table 1. An overview of experimental designs.

Experiment	Integrations	Descriptions	Period
Historical	1	CMIP5 historical simulation	1850-2005
RCP45	1	CMIP5 RCP4.5 scenario	2006-2100
RCP85	1	CMIP5 RCP8.5 scenario	2006-2100
CCT	3	RCP8.5 scenario with thinner cirrus clouds, which results in lowering global mean temperature	2020-2100
CCText	1	An extended 50-year simulation after termination of the CCT technique	2101-2150
MSB	3	RCP8.5 scenario with larger sea salt emission from ocean surface within 45°S-45°N; a higher sea salt concentration makes the lower atmosphere and stratiform clouds over ocean brighter, thus the surface albedo increases and the surface temperature falls	2020-2100
MSBext	1	An extended 50-year simulation after termination of the MSB technique	2101-2150
SAI	3	RCP8.5 scenario with an additional surface layer in the stratosphere that reflects incoming solar radiation, thereby inducing surface cooling	2020-2100
SAIext	1	An extended 50-year simulation after termination of the SAI technique	2101-2150

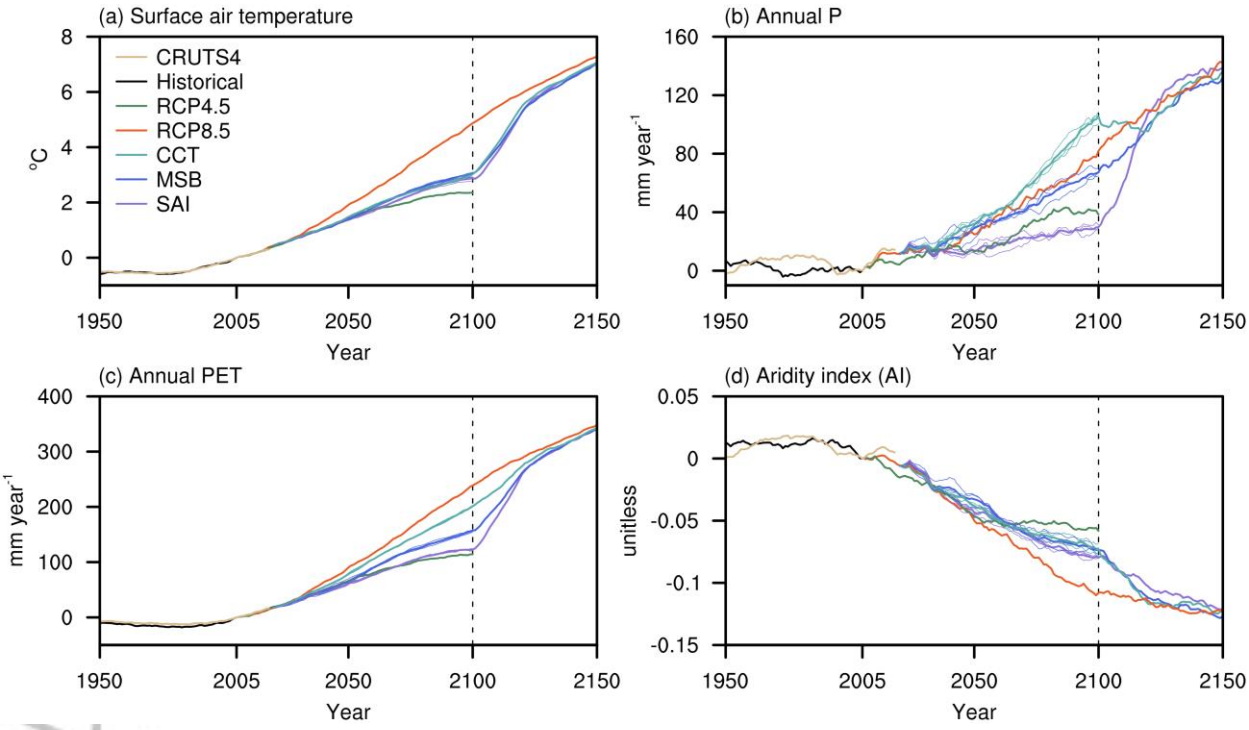

Figure 1. Temporal changes in 20-year running mean (a) surface air temperature, (b) annual P and (c) PET, and (d) aridity index relative to the 1986-2005 climatology. Individual variables are averaged over the land surface within the latitudes of 60°S-60°N. Ivory, black, green, red, cyan, blue, and purple lines indicate CRUTS4, Historical, RCP4.5, RCP8.5, CCT, MSB, and SAI, respectively. For CCT, MSB, SAI, thin lines denote individual experiments, and their ensemble means are denoted by thick lines.

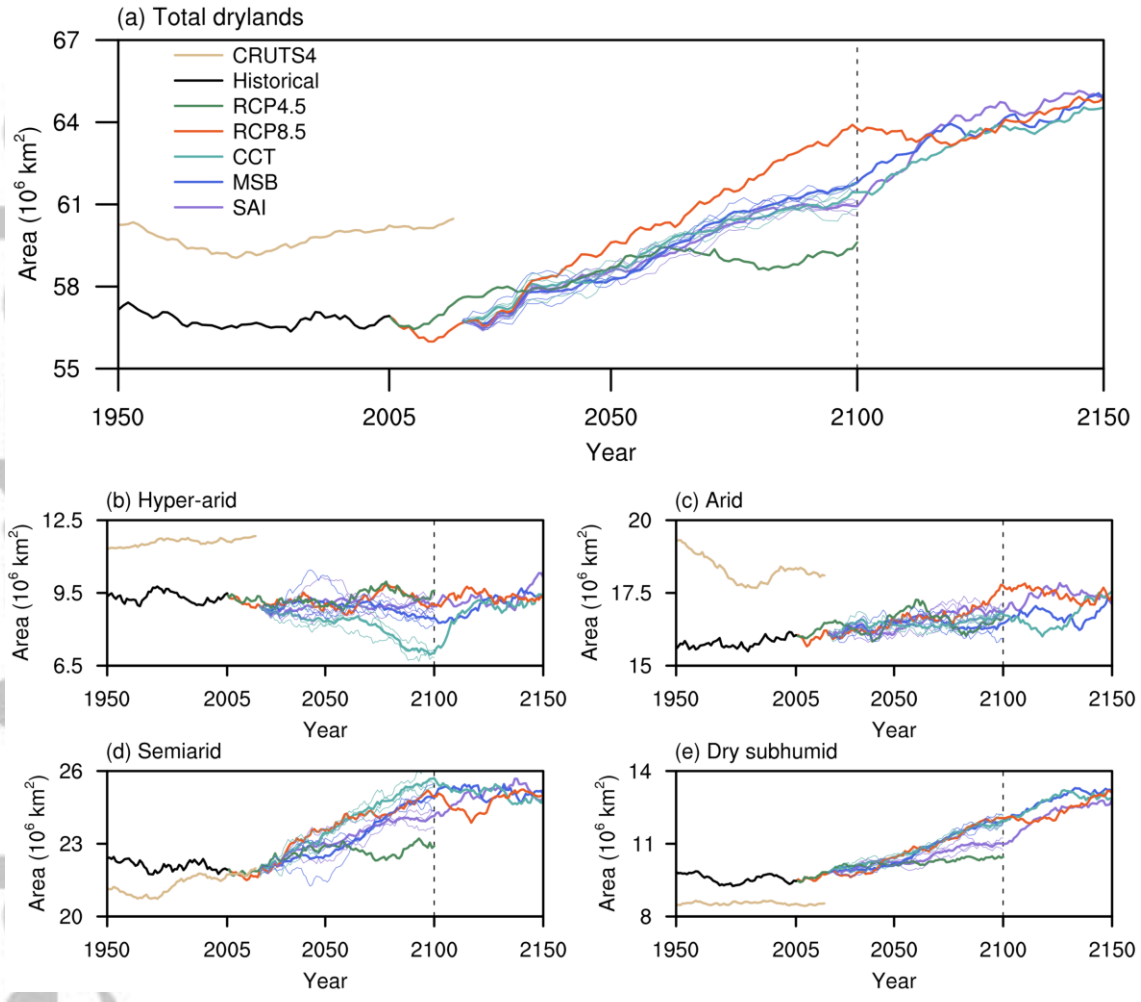

Figure 2. Time series of 20-year running mean areas of (a) total drylands, (b) hyper-arid, (c) arid, (d) semiarid, and (e) dry subhumid regions. Ivory, black, green, red, cyan, blue, and purple lines indicate CRUTS4, Historical, RCP4.5, RCP8.5, CCT, MSB, and SAI, respectively. For CCT, MSB, and SAI, thin lines denote individual experiments, and their ensemble means are denoted by thick lines.

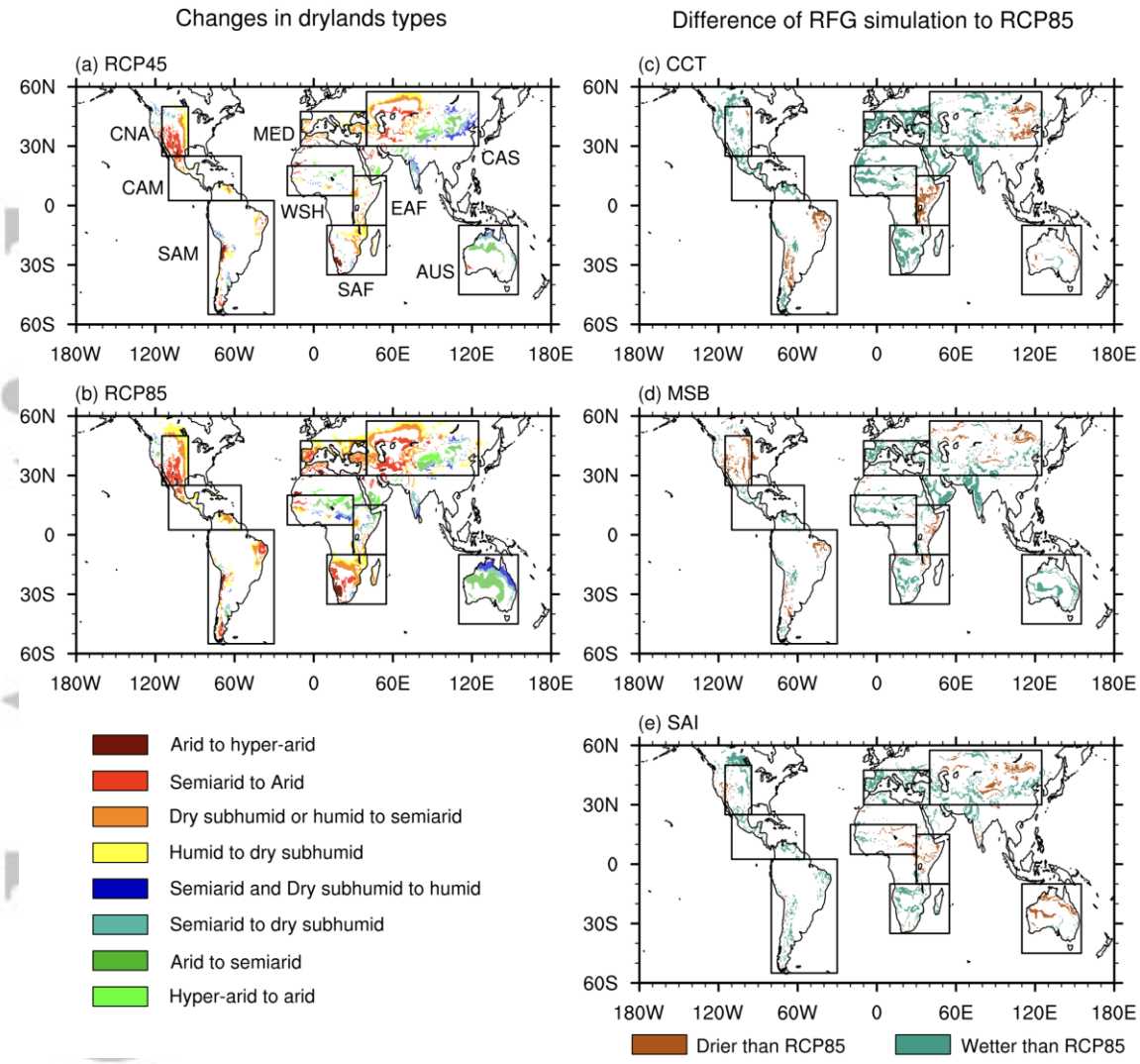

Figure 3. Global distributions of dryland type changes to drier and wetter in 2081-2100 relative to 1986-2005 from (a) RCP4.5 and (b) RCP8.5. Drylands type changes to drier and wetter relative to RCP8.5 under (c) CCT, (d) MSB, and (e) SAI for the period of 2081-2100. For CCT, MSB, and SAI, the ensemble mean is used to determine dryland type changes.

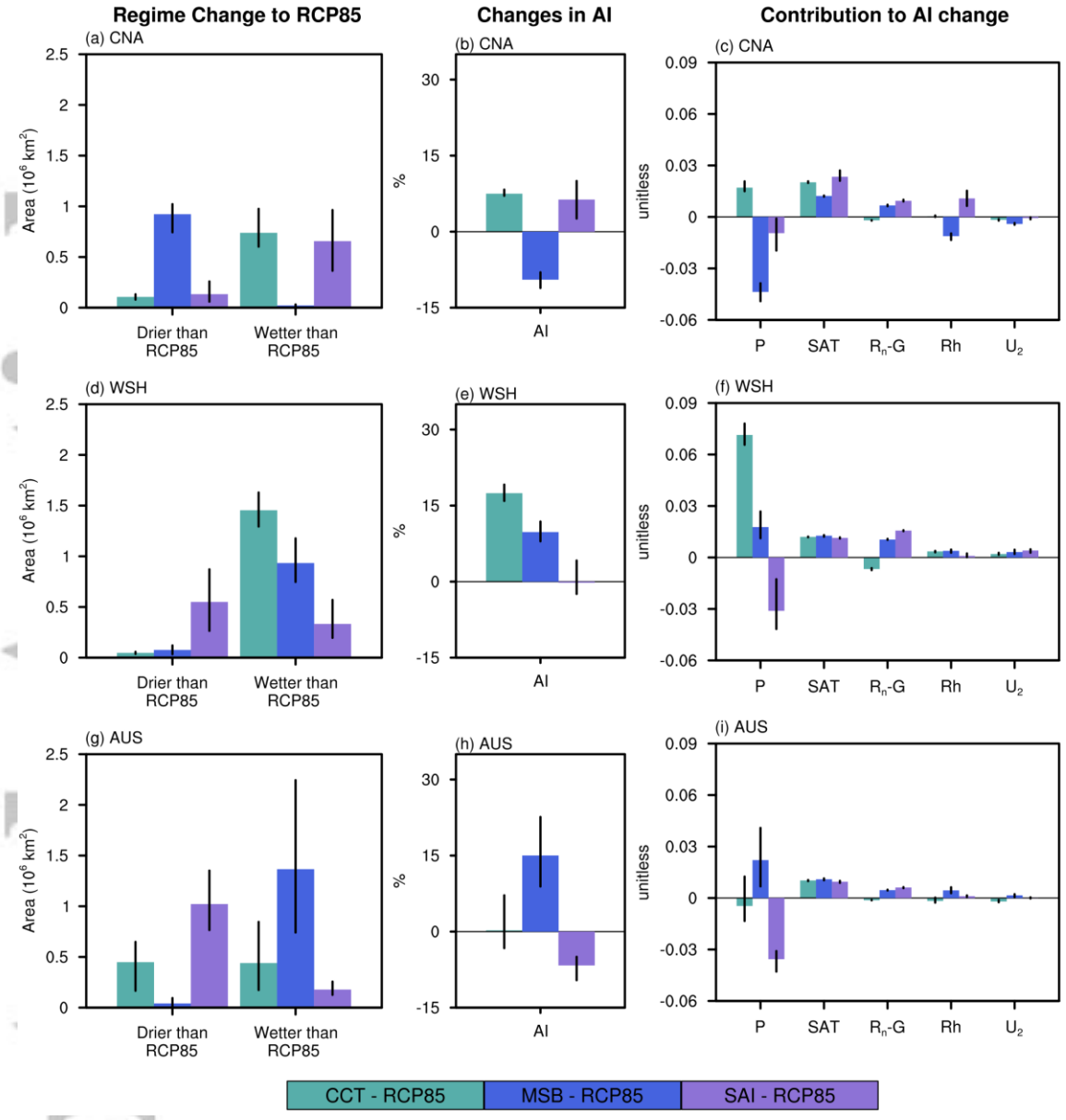

Figure 4. (a) Area of type changes to drier and wetter relative to RCP8.5 in 2081-2100, (b) changes in aridity index (AI) in 2081-2100 relative to 1986-2005, and (c) relevant contributions of precipitation (P), surface air temperature (SAT), available energy (R_n–G), relative humidity (Rh), and wind speed (U_2) to the AI changes over central North America (CNA). (d), (e), and (f) same as (a), (b), and (c), but over western Sahel (WSH). (g), (h), and (i) same as (a), (b), and (c), but over Australia (AUS). Cyan, blue, and purple bars indicate the ensemble mean difference of CCT, MSB, and SAI to RCP8.5, respectively. Black solid lines denote the maximum-minimum range of the differences.